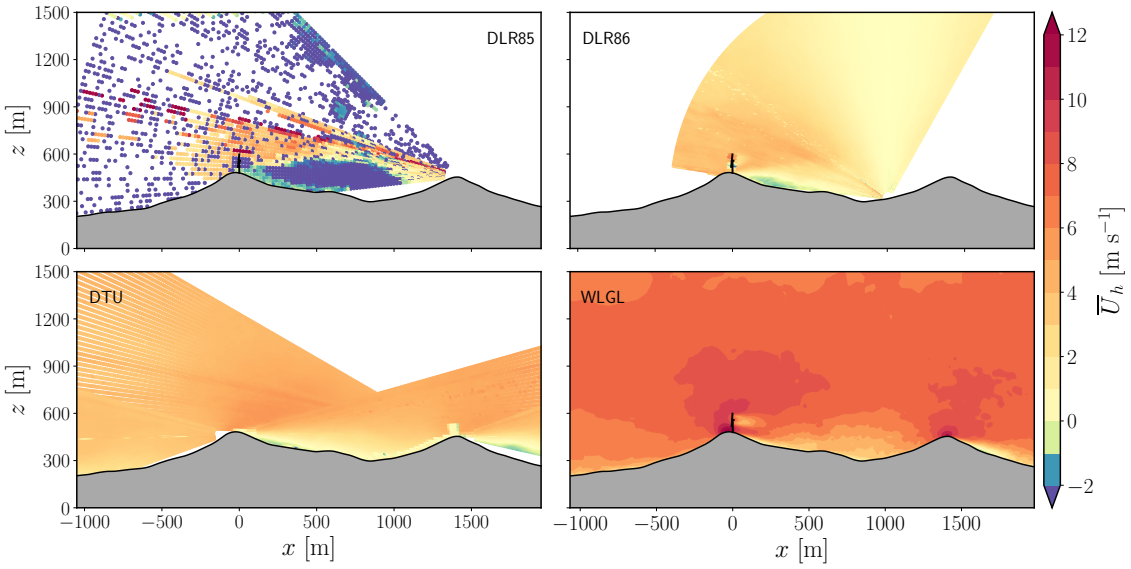

Figure 8.23: Same as in Figure 8.22, but for the unstable case.

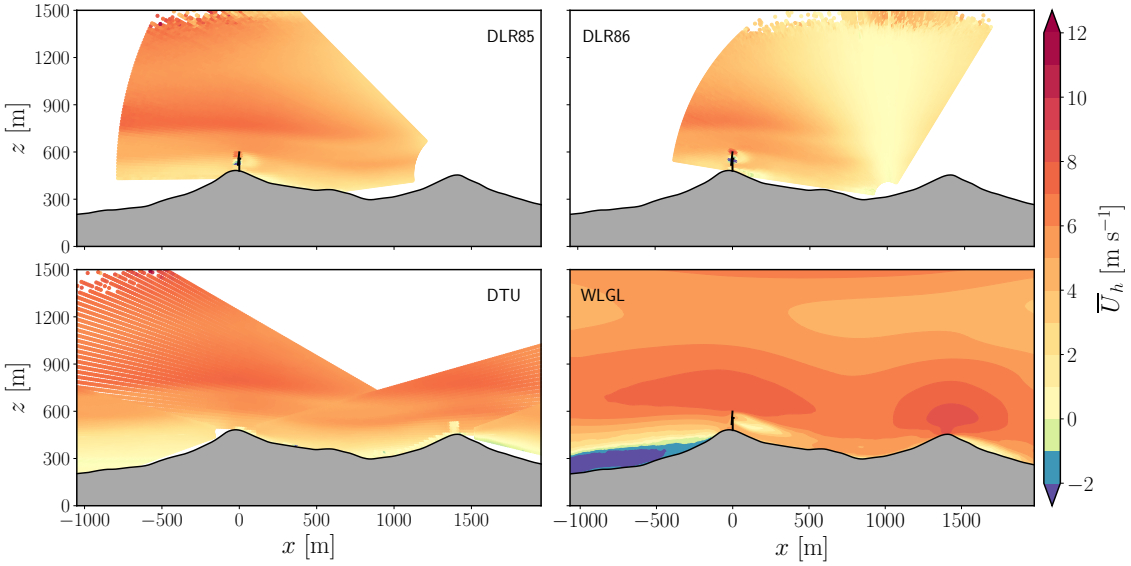

Figure 8.24: Same as in Figure 8.22, but for the stable case.

near hydrostatic equilibrium where the vertical accelerations associated with the flow are relatively small [330].

Figure 8.25 shows the locations and corresponding velocity deficit profiles from DLR lidars, and the results from the WLGL model. In order to obtain such vertical profiles, lidar data were interpolated into the model's wake transect plane. The dashed black line denotes the velocity deficit profile at $1D$ upstream of the wind turbine. Mean wake velocity deficit ($\overline{VD}$) profiles that are plotted as a function of nondimensional height, $(z - z_{hub})/D$, are obtained using Equation (7.7).

For the neutral ABL conditions, 1-hour average $\overline{VD}$s from the lidars and the model cannot be compared directly, as there is an upward drift ($\sim$20 m at $x/D = 0.5$) in the observed

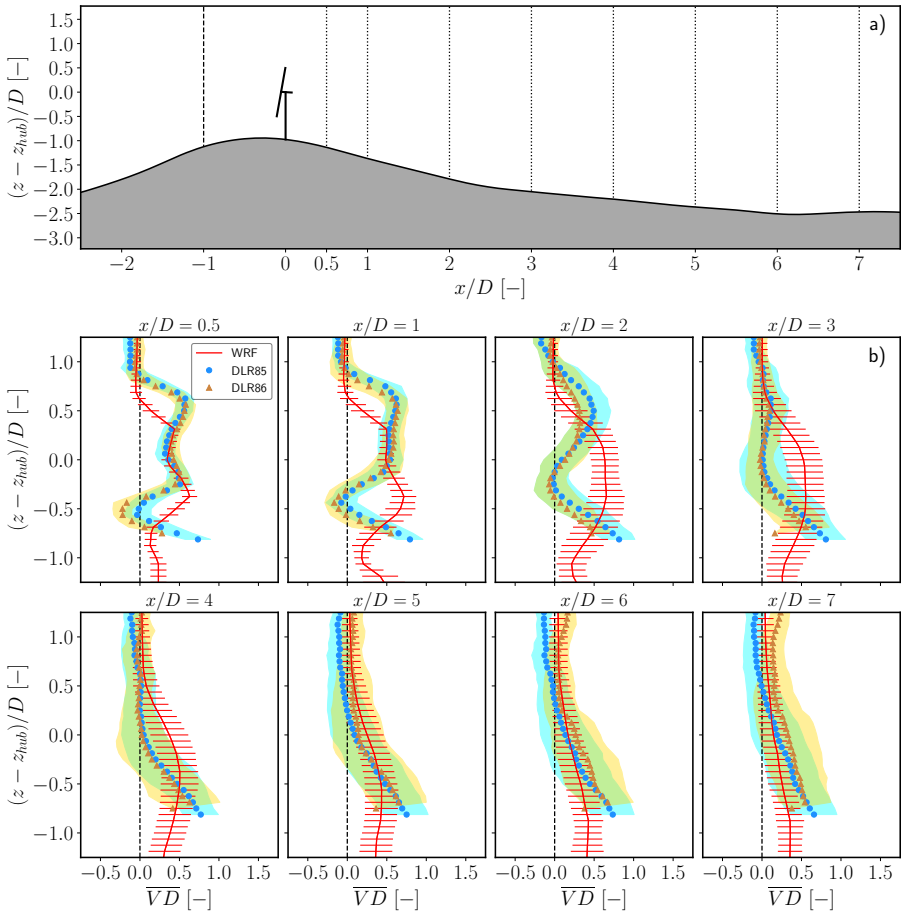

Figure 8.25: (a) Locations of the corresponding mean wake velocity deficit ($\overline{VD}$) profiles shown below, as a function of nondimensional height, with z_{hub} and D being the hub height and rotor diameter, respectively. The dashed black line indicates the inflow location, whereas the black dotted lines represent different leeward locations from the mountain top into the valley (a). 1-hour average wake velocity deficit profiles obtained from WLGL simulation and DLR lidars at different downstream locations of the wind turbine (b). (—) indicate the standard deviation around the mean $\overline{VD}$ value. (▭) and (▭) shaded regions cover the mean ± standard deviations of $\overline{VD}$ during the 1-hour averaging period of the simulation results and measurement data, respectively. The results correspond to the neutral case.

wake (Section 8.1.6). However, a similar flow deceleration in wake velocity is observed both in the experiments and in the results from the numerical model, up to $1D$, but the modeled wake stretches further downstream. The modeled far wake $\overline{VD}$s match reasonably well and lay in the region covering the mean ± standard deviations of $\overline{VD}$, although $\overline{VD}$ profiles are slightly different. Nacelle and tower have no significant impact on both the modeled and measured wake velocity deficit profiles.

Similar to the neutral ABL conditions, an upward shift of about ~ 15 m at $x/D = 0.5$ was observed in the near wake captured by DLR86 lidar under unstable ABL conditions (Figure 8.26). In contrast to the near wake predictions of the WLGL model under neutral ABL conditions, the modeled wake closely resembled the one observed in the DLR86 lidar scan. This alignment was attributed to increased surface heating, which contributed to

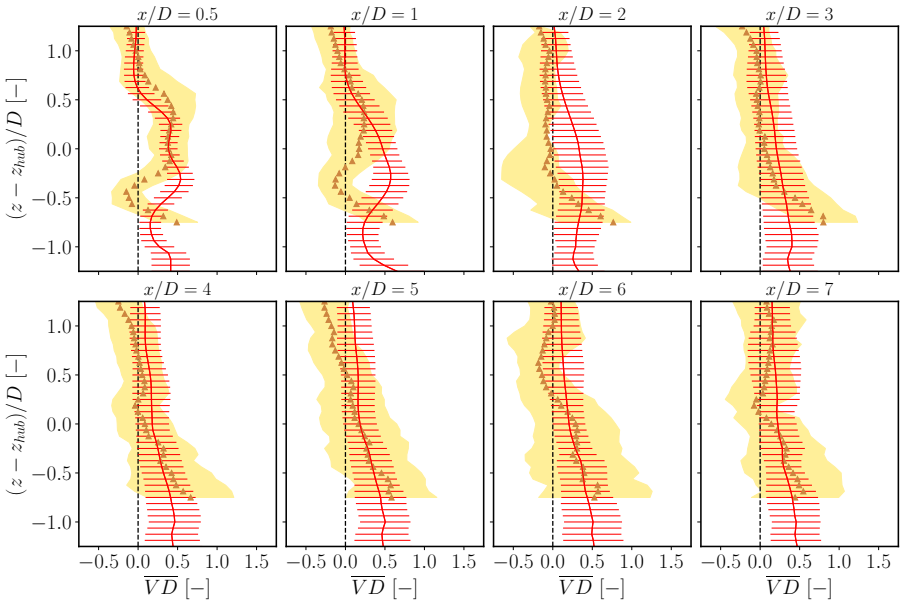

Figure 8.26: Same as in Figure 8.25, but for the unstable case.

buoyancy generation and, consequently, the vertical displacement of the wake. On the other hand, the enhanced vertical mixing resulted in faster attenuation of the far wake than that observed in the neutral ABL conditions. The modeled wake persists up to $\sim 2D$, whereas the observed wake disappears approximately at $\sim 1D$. Interestingly, the aerodynamic effect of the wind turbine tower was evident in the modeled near wake at $x/D = 0.5$ and $x/D = 1$, as it created an extra velocity deceleration below the hub height. However, the tower did not significantly contribute to the mean wake velocity deficit measured by the DLR86 lidar.

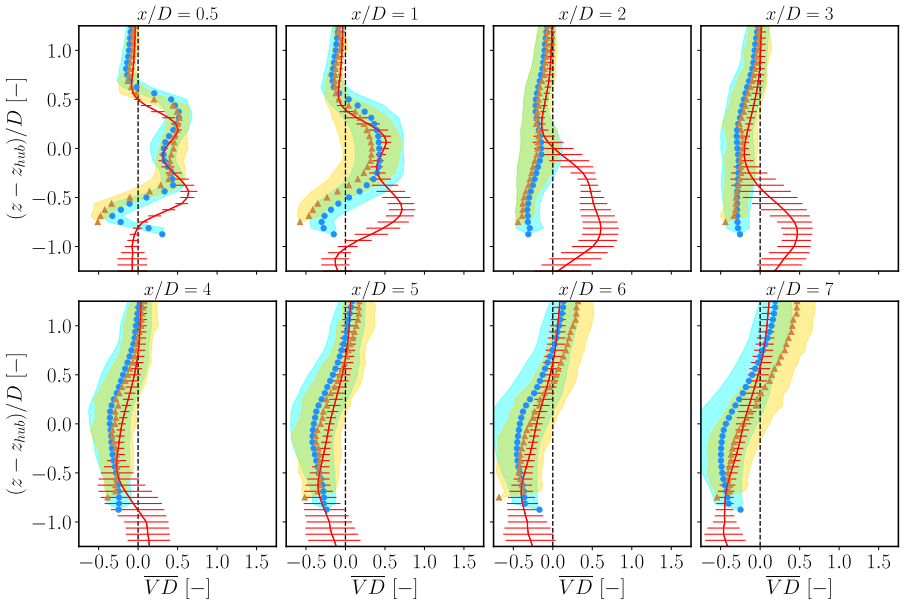

Figure 8.27: Same as in Figure 8.25, but for the stable case.

Figure 8.27 shows a comparison of time-averaged modeled and observed wake velocity

deficit profiles, $\overline{VD}$, at different locations downstream of the wind turbine for the stable case. Unlike the upward shift of the wake observed in other stability conditions, no vertical displacement was observed in $\overline{VD}$ at $x/D = 5$, yielding a better match between the observed and modeled wake velocity deficit profiles in the near wake. In contrast, the modeled wake persisted more into the valley and began to dissipate after $x/D = 4$, whereas the observed wake began to dissipate just after $x/D = 2$. Further downstream, the shape became less circular, and the velocity deficit gradually decreased.

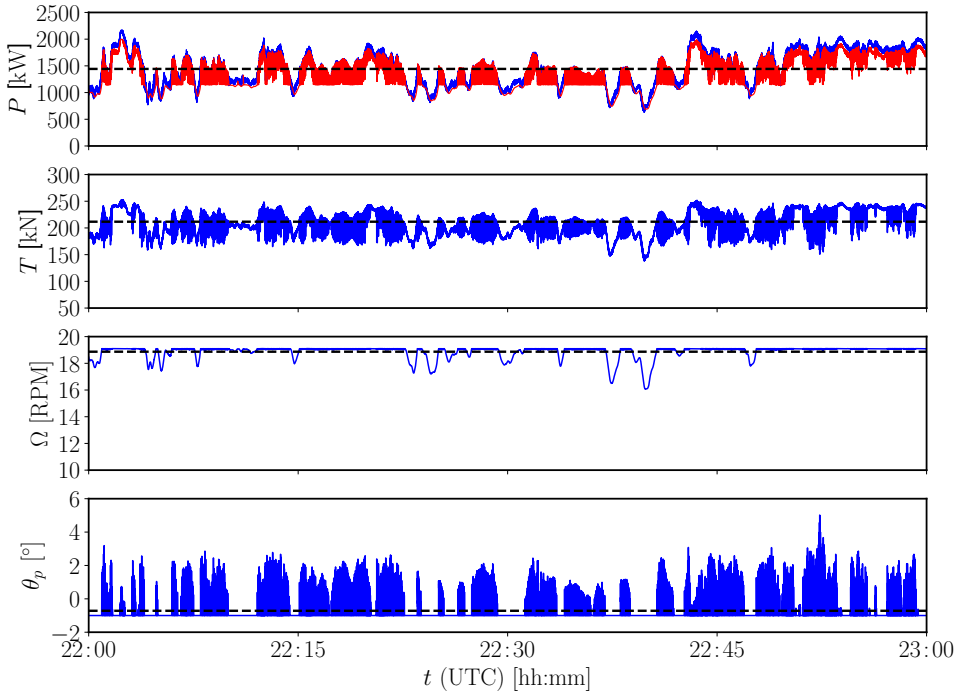

Figure 8.28: Time series of power, P, thrust, T, rotational speed, Ω, and pitch angle, θ_p, of the generic Vestas V80 wind turbine represented by the WLGL model. (——) corresponds to the WLGL model estimations for aerodynamic power and thrust, and pitch angle, while (——) denotes the WLGL model estimations for generator power. (- - -) denotes the mean values over the period of interest. The results correspond to the neutral case.

Figure 8.28 presents time series of wind turbine rotor and generator power, thrust, rotational speed, and pitch angle over the simulated 1-hour period under neutral ABL conditions. The 1-hour average aerodynamic power is about 1443 kW, the generator power is $\sim$1341 kW, the rotor speed is 18.9 RPM, and the blade pitch angle is about $-0.72°$. The mean aerodynamic thrust is found to be 221.770 kN. Compared to the power and thrust curves of the generic Vestas V80 reported by Churchfield [54] in Figure 8.4, a positive bias of about 0.05 in mean thrust coefficient, $\overline{C}_T$, 0.12 in mean aerodynamic power coefficient, $\overline{C}_{P_r}$, and 0.11 in mean generator power coefficient, $\overline{C}_{P_g}$, at an average wind speed of 9.5 m s^{-1} and air density of 1.15 kg m^{-3} is observed.

For the unstable case results shown in Figure 8.29, the modeled mean aerodynamic power is about 1332 kW, the generator power is $\sim$1239 kW, the rotor speed is 18.1 RPM, and the blade pitch angle is about $-0.66°$. The mean aerodynamic thrust is found to be

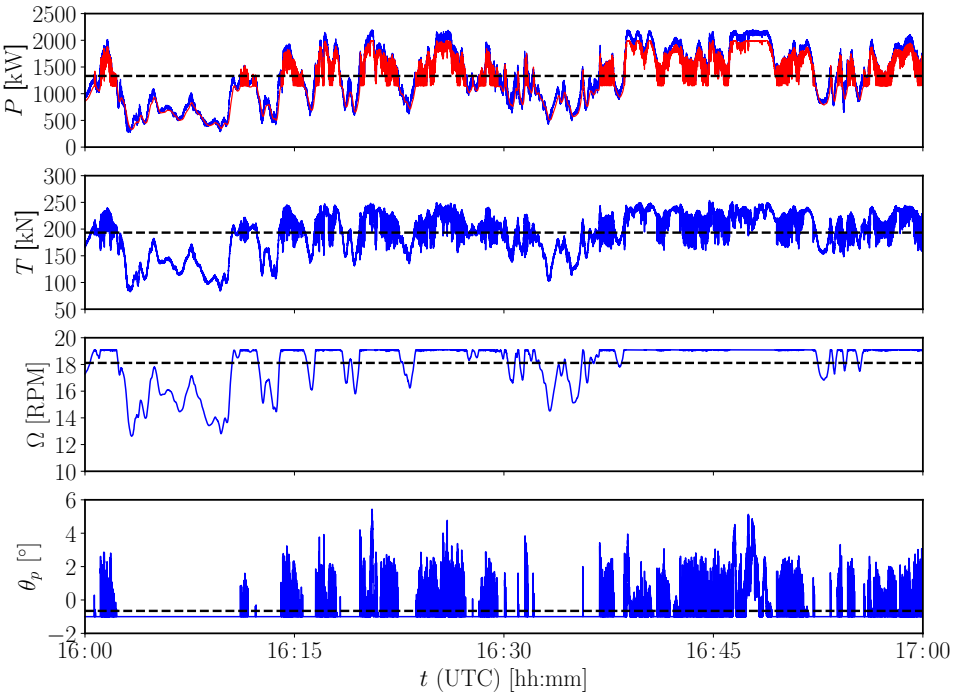

Figure 8.29: Same as in Figure 8.28, but for the unstable case.

193.381 kN. A positive bias of about 0.086 in mean thrust coefficient, $\overline{C}_T$, 0.17 in mean aerodynamic power coefficient, $\overline{C}_{P_r}$, and 0.16 in mean generator power coefficient, $\overline{C}_{P_g}$, at an average wind speed of 9.1 m s^{-1} and air density of 1.12 kg m^{-3} is observed.

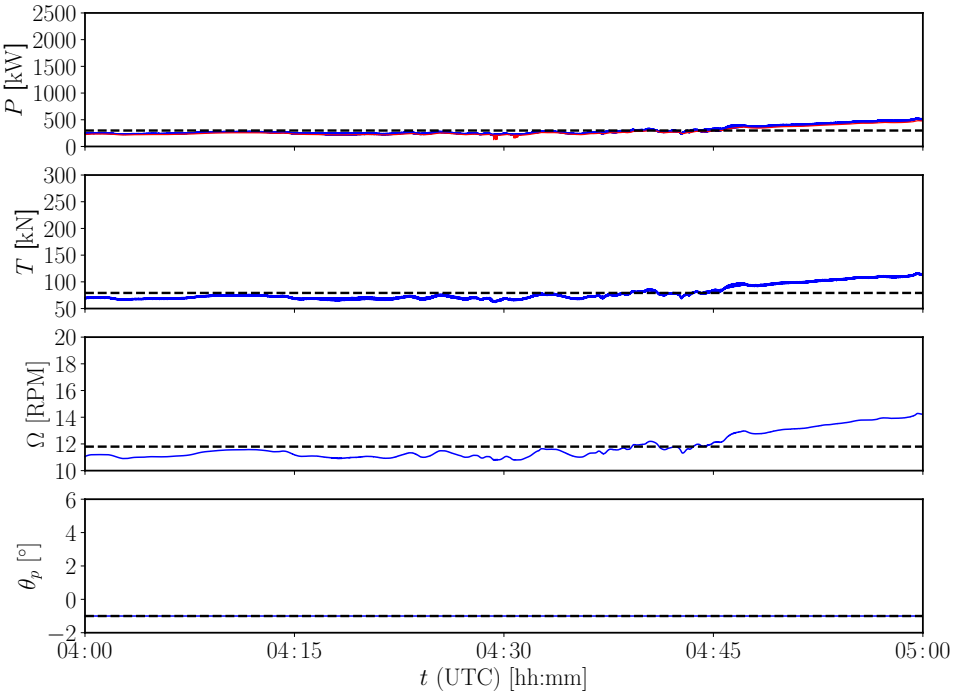

Figure 8.30: Same as in Figure 8.28, but for the stable case.

For the stable case, the modeled mean aerodynamic power is about 339.3 kW, the generator power is ∼315.7 kW, the rotor speed is 12.4 RPM, and the blade pitch angle is −1° (see

Figure 8.30). The mean aerodynamic thrust is found to be 86.229 kN. A positive bias of about 0.17 in mean thrust coefficient, $\overline{C}_T$, 0.18 in mean aerodynamic power coefficient, $\overline{C}_{P_r}$, and 0.17 in mean generator power coefficient, $\overline{C}_{P_g}$, at an average wind speed of 5.7 m s^{-1} and air density of 1.13 kg m^{-3} is observed. The aerodynamic power and thrust outputs were almost constant until 04:45 (UTC) but began to increase thereafter, primarily driven by the rise in predicted inflow wind speed.

For the neutral and unstable cases simulated, when the rotor speed exceeded the rated rotor speed, that is $\Omega_R = 19.1$ RPM, the generator speed controller algorithm was activated and the rotor speed was maintained at the rated rotor speed. The blade pitch angle was then adjusted to reduce the aerodynamic load on the wind turbine blades. The blade pitch controller was never activated during the WLGL simulation of the stable case because of very low inflow wind speeds.

8.1.7 Conclusions

In order to investigate the impact of uncertain weather conditions on the wake behavior and aerodynamic performance of an isolated wind turbine operating on top of the southwest ridge of Perdigão Valley, large-eddy simulations of neutral, unstable, and stable atmospheric boundary layer flow in the complex terrain of Perdigão have been performed using a combination of the Weather Research and Forecasting-Large Eddy Simulation-Generalized Actuator Line models (WRF-LES-GAL or WLGL). The simulated flow field results have been compared with existing experimental data from the Perdigão experimental campaign.

Numerical results from the met masts have shown that the time series and vertical profiles of horizontal wind speed, wind direction, potential temperature, the Obukhov length, and turbulence intensity agree reasonably well with experimental data, despite minor differences in the vertical profiles of horizontal wind speed over the ridges and wind direction in the valley. For all the atmospheric stability cases tested, the WLGL model overestimates the 1-hour average horizontal wind speed at hub height on the order of 1-5 m s^{-1} over the ridges (TSE04 and TSE13) and within the valley (TSE09). The predicted 1-hour average bias between WRF-LES and measurements of wind direction at hub height varies between $-4.8°$ and $29.3°$ over the ridges, and between $25.4°$ and $83.09°$ within the valley, respectively, for the three atmospheric stability conditions. For the potential temperature gradient, the 1-hour average bias error is quite small and ranges from -0.007 K m^{-1} to 0.035 K m^{-1} on the SW and NE ridges, yet it is negatively biased in the valley on the order of -0.0165 K m^{-1}, -0.0046 K m^{-1}, and -0.0233 K m^{-1} for the neutral, unstable, and stable cases, respectively. For turbulence intensity, a reasonably better match, e.g., with a hub height bias error of about $\overline{TI}_{hub} \approx 0.1$ on the ridges and $\overline{TI}_{hub} \approx 0.2$ within the valley, is observed at different measurement locations, compared to other vertical profiles analyzed, for the three atmospheric stability cases.

For all stability conditions, the simulated wake was not entirely aligned with the vertical

scan planes of the DLR lidars. Besides, the wake was deflected after a few rotor diameters downstream, towards the north of the DLR lidars, making the comparison of modeled wake behavior with lidar data difficult. Apart from that, wind turbine's aerodynamic behavior agrees fairly well with the power and thrust data given in Figure 8.4. Spectra and co-spectra of various quantities show that the current WLGL setup is a promising approach to capture transient turbulent flow structures, as well as microscale flow features that are important in wake modeling, despite the shortcomings explained previously. Overall, the WLGL model is able to reproduce the wake characteristics observed on top of the first ridge into the valley, as well as the power and thrust generation.

8.2 Flat terrain: The Høvsøre benchmark

In order to investigate the aeroacoustic performance of a real-scale wind turbine under realistic mesoscale forcing, a period with unstable ABL conditions, observed at the Danish National Test Center for Large Wind Turbines at Høvsøre, Denmark, which is located in a relatively flat terrain by the western coast of Jylland, was chosen (Figure 8.31). The WLGL model is utilized in order to simulate the period of interest with a multi-scale modeling approach, as in Section 8.1. Five nested domains, with the finest domain having a spatial resolution of 3 m, are used to dynamically downscale mesoscale flow features to the microscale domain. The WLGL model results have been compared with the available experimental data from a met mast located a few meters downstream of the wind turbine.

For the aeroacoustic modeling of the wind turbine considered in this work, an explicit coupling strategy between the WLGL model and a semi-analytical noise model, described in Section 5.3, has been implemented. As a first step, the results from the WLGL model are obtained performing multi-scale WRF-LES simulations with realistic atmospheric forcing under unstable ABL conditions of the Siemens 2.3 MW 93m rotor diameter WT installed in the test site (Figure 8.32). Then, these data are introduced as inputs in a realistic trailing-edge noise model. The design and operational data of the SWT-2.3-93 WT are obtained from the literature and experiments conducted during the Høvsøre experimental campaign in 2006.

This section is organized as follows: Section 8.2.1 introduces the motivation of this study, including a brief introduction. It is followed by a short description of the Høvsøre field campaign (Section 8.2.2). After, the content is split into three parts as: Part I – atmospheric flow modeling (Section 8.2.3), Part II – wind turbine wake modeling and power estimation (Section 8.2.4), and Part III – aeroacoustic modeling of the wind turbine (Section 8.2.5). The results based on the aerodynamic and aeroacoustic response of the SWT-2.3-93 WT are given separately. Conclusions are drawn at the end of this chapter (Section 8.2.6).

This section utilizes the material from an article that is presently being prepared for submission to an international peer-reviewed journal:

- Kale, B., Kucukosman, C., Christophe, J., Schram, C., van Beeck, J. and Cuerva-Tejero, A., 2023. Towards a more realistic trailing-edge noise modeling of a full-size wind turbine operating in unstable ABL conditions. *Wind Energy Science* (in preparation).

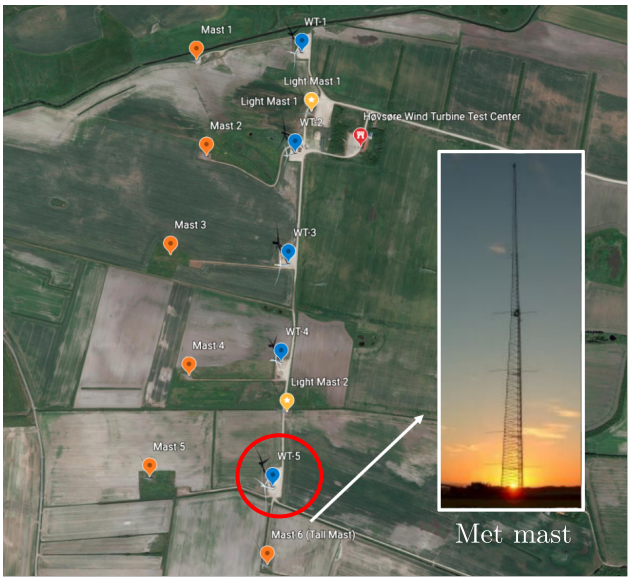

Figure 8.31: A screenshot from Google Earth satellite imagery of Høvsøre, Denmark. The layout of the Høvsøre site shows the locations of the wind turbines and the instrumentation installed in the test site. The wind turbine considered in this work is encircled by the red circle. Experimental data was collected from a 116.5 m met mast shown in a white box. Met mast locations are marked by orange and yellow pins, whereas wind turbine locations are indicated by blue pins.

Figure 8.32: A picture of the SWT-2.3-93 WTs installed in the Høvsøre test site. The wind turbine considered in this work is encircled by the red ellipse. Reproduced from: DTU [83].

8.2.1 Motivation

Wind turbine noise emissions have become an essential factor to be considered in the deployment of WT technology. The power generation and noise level produced by wind turbines can vary depending on several factors, including the type and size of the wind turbine, inflow wind speed and wind direction, the distance between the wind turbine and the observer, and terrain type among others. Flat terrains are generally preferred for wind turbine installations, due to ease of construction and relatively less turbulent wind flow patterns, as opposed to complex terrain where the topography is not uniform as well as the land cover [270]. Flat areas without vegetation are ideal for ambient noise measurements because these locations lack significant background noise sources, such as forests, tall

vegetation, and other factors that contribute to increased atmospheric turbulence [350]. Measuring wind turbine noise in flat terrain can yield valuable data for designing quieter wind turbines, thereby reducing the environmental and human health impact of these turbines.

The primary purpose of the WLGL model is to replicate the aerodynamic effects of wind turbines under realistic atmospheric turbulence conditions. Nevertheless, it can also be employed to provide the necessary input data for aeroacoustic solvers. Thereby, this study is devoted to analyzing the effectiveness of mesoscale microscale wind turbine coupling for noise modeling (MMWTC-NM) chain described in Section 1.3, which incorporates an explicit coupling of the WLGL model with a RANS solver and a semi-analytical noise model, in reproducing the noise emitted by a large onshore wind turbine operating in the atmospheric boundary layer, taking into account the effects of wind flow non-uniformity to which the wind turbine is exposed in reality.

The Høvsøre test site is a well-known facility in Denmark used to conduct wind turbine power and noise measurements according to international technical regulations, such as the International Electrotechnical Commission (IEC) Standard. A large number of measurement stations, including met masts and lightning towers, are installed at different distances from the turbines at the facility. At these stations, advanced equipment is installed to measure the weather conditions and the sound levels produced by the wind turbines in various locations in their surroundings.

8.2.2 The Høvsøre test site experiments

The Høvsøre wind field experiment in 2006 was conducted, as part of a project supervised by Ejler Kristensen from Siemens Wind Power A/S, to measure the noise print of a Siemens 2.3 MW wind turbine in flat and uniform terrain [183]. The two-day field campaign took place in the coastal area of Høvsøre, Denmark, from May 30$^{\text{th}}$ to May 31$^{\text{st}}$ in 2006.

The main goal of the experimental campaign was to perform noise measurements of a real-scale wind turbine operating in the atmospheric boundary layer, using different pitch angles and rotational speed configurations. The two closest wind turbines (and the farthest) were shut down during the experimental campaign for maintenance work. Although the fourth wind turbine was operational during the measurement process, it was too far from the wind turbine under test; therefore, it did not affect the measurements. The noise data, collected by the Brüel and Kjær microphones and the software PULSE during the experiment [36], were also used to validate and improve numerical models applied to predict wind turbine noise in wind energy applications. In addition, data from the wind turbine, such as power, pitch and yaw angles, as well as rotor and generator speed, were also recorded simultaneously to the noise measurements. However, these data are not publicly available. Noise measurements were carried out simultaneously at four locations, including 100 m downwind, 150 m downwind, 20 m in the rotor plane, and 150 m in the rotor plane [183]. All distances were measured from the tower base. Only measurements

Table 8.4: Instrumentation on the Høvsøre mast in Denmark [261].

Sensor type	Instrument	Height [m]
Wind speed	Risø P2546A cup anemometer	$2, 10, 40, 60, 80, 100$, and 116.5
Wind direction	Risø P2021A wind vane	$10, 60$, and 100
Relative humidity	F2920A Väisälä HMP45A RH/ T probe radiation shield	2 and 100
Temperature gradient	Risø P2642A sensor/ Risø P2029 radiation shield	$2, 40, 60, 80$, and 100 (relative to the lowest level)
Temperature (absolute)	Risø P2449A sensor/ Risø P2029 radiation shield	$-0.05, 2$, and 100
Pressure	P2717A Väisälä barometer PTB100	2 and 100
Turbulence	Metek USA1 F2901A sonic	$10, 20, 40, 60, 80$, and 100
Solar radiation	F2253C CM11 pyranometer	2

collected at 100 m downwind of the wind turbine are analyzed in this dissertation. The noise results are reported in the third-octave band with an A-weighting filter. The sound power level, SWL or L_w, is obtained as

$$L_w = L_p + 10 \log_{10} \left(4\pi R^2\right), \tag{8.2}$$

where L_p is the sound pressure level at the observer location (based on a reference pressure of 20 μPa) and R is the distance between the rotor center and microphone position. As reported in Leloudas [183], the measured L_w data were further corrected by simply adding -6 dB to account for a fully reflective surface (hard ground).

During the field campaign, the wind speeds at Høvsøre were not very high; therefore, it was possible to collect high-quality experimental noise data. Due to the relatively low wind speed levels, the noise emitted from the wind turbine was not masked by leaves, trees, and sea waves. Nevertheless, the wind conditions varied across the different measurement series. On the first day, the average wind speed was about 8.5 ± 1.7 (standard deviation) m s^{-1}, whereas much lower wind speeds were observed during the second day (i.e., 5.6 ± 1.4 m s^{-1}). The wind speed accelerated later in the afternoon, resulting in an average wind speed of about 9.8 ± 1.9 m s^{-1} [183].

The weather data and relevant atmospheric parameters were also collected by experimental means, including sonic and cup anemometers, and wind vanes mounted on a 116.5 m tall met mast, also known as the Høvsøre mast, at varying heights (see Table 8.4). The weather data collected by the instruments were recorded and processed in real-time; the results were analyzed to provide valuable insight into the characteristics of the turbulent wind field. The weather data collected from the Høvsøre mast, have also been used for many years to help improve the accuracy and reliability of numerical models used in wind resource assessment and wind power applications at Høvsøre, as well as in the design and operation of wind turbines, and to explore ways to increase the efficiency and reliability of wind power systems.

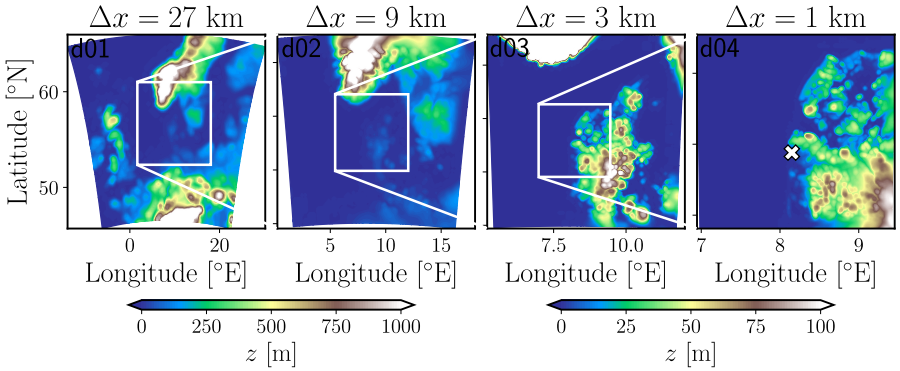

Figure 8.33: Nested domain configuration from the mesoscale WRF simulation. All nested domains centered on the Høvsøre test site are colored by terrain height where $z = 0$ m corresponds to sea level. The four domains have resolutions of 27 km, 9 km, 3 km, and 1 km, respectively. Domain dimensions and other model configuration parameters are given in Table 8.5.

8.2.3 Part I – Atmospheric flow modeling

Prior to conducting an in-depth analysis of the aerodynamic and aeroacoustic performance of the SWT-2.3-93 wind turbine installed in the Høvsøre test site, it is essential to accurately model the mesoscale flow conditions for the chosen time stamp. This accurate modeling is crucial for minimizing the model's prediction error. The bias between the measured and simulated atmospheric quantities is highly dependent on the capability of the mesoscale models, as these models are sensitive to grid resolution, physics schemes, as well as the initial and lateral boundary conditions provided by reanalysis datasets [96]. Siuta et al. [302] concluded that choosing the best planetary boundary layer (PBL) scheme and grid resolution configuration may improve model predictions and decrease the mean absolute errors by up to $\sim 30\%$. Even when using finer microscale domains in a nested mesoscale-microscale configuration where the grid resolution is refined through the microscale domains, it does not guarantee the lowest errors or the best results if the initial and lateral boundary conditions, or physical schemes, are improperly selected [249].

WRF model sensitivity to reanalysis dataset and PBL schemes

The sensitivity analysis described herein involves examining the response of the model output to changes in the input parameters. This type of analysis can help identify the most critical input parameters affecting the model's performance and provide insight into the underlying physical processes in order to perform reliable ABL flow simulations. When performing multi-scale simulations of atmospheric flows in wind energy studies, it is necessary to produce reliable and accurate ABL flow simulations for all domains from mesoscale to microscale.

A numerical error produced by any physical schemes used in multi-scale flow modeling can propagate across the nested domains, resulting in larger bias errors in atmospheric quantities in microscale flow analysis. This can cause further problems in the aeroacoustic

Table 8.5: Domain dimensions and model configuration parameters for the sensitivity analysis of the ABL flow in the flat terrain of Høvsøre.

Domain	$N_x \times N_y \times N_z$	Δx [m]	Δz [m]	Δt [s]	Spin-up [hour]
d01	$81 \times 81 \times 58$	27000	~ 4	45	12
d02	$109 \times 109 \times 58$	9000	~ 4	15	12
d03	$133 \times 133 \times 58$	3000	~ 4	5	12
d04	$151 \times 151 \times 58$	1000	~ 4	5/3	12

Note. N_x, N_y, and N_z stand for the number of grid points whereas $\Delta x, \Delta y$, and Δz represent the spatial grid resolutions in the x, y, and z directions, respectively. Note that $\Delta x = \Delta y$ and Δz is set close to the values given in the table, because of WRF's terrain-following vertical coordinate system in the vertical direction. Δt is the computational time step size.

modeling of the wind turbines, as the aerodynamic load will likely be incorrectly estimated.

With this regard, a sensitivity analysis based on four different PBL models, namely MYJ, MYNN, S-H, and QNSE, forced two different reanalysis datasets, namely ERA5 and GFS, was conducted to evaluate the accuracy of the WRF model in terms of factors, such as horizontal wind speed, U_h, wind direction, β, and temperature, T, at 80 m. The spatial and temporal resolutions of these datasets are as follows: $0.1^\circ \times 0.1^\circ$ and 1-hour for the ERA5 and $1^\circ \times 1^\circ$ and 6-hour for the GFS reanalysis datasets, respectively.

Time series of above-mentioned atmospheric quantities were saved every 10-min and compared with 10-min average weather data collected from the Høvsøre mast between 30/05/2006 12:00 (UTC) and 31/05/2006 18:00 (UTC), yielding a total analysis time of 30 hours. The WRF results from the finest domain have been interpolated to the Høvsøre mast location for comparison with the experimental data. Bi-linear and linear interpola-

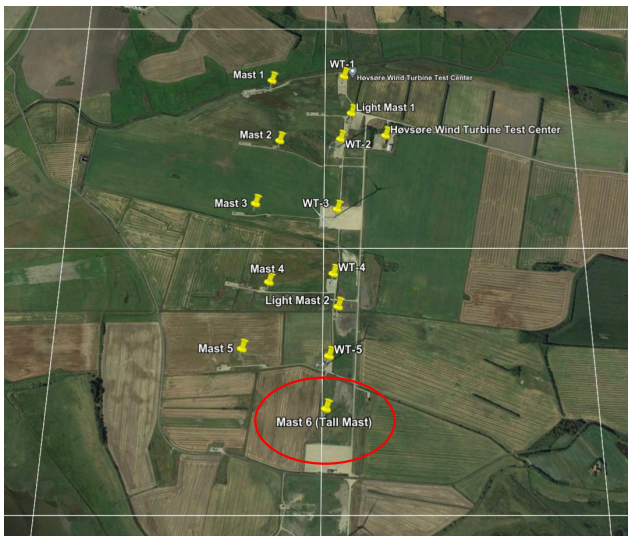

Figure 8.34: A screenshot from Google Earth satellite imagery of Høvsøre, Denmark, with wind turbines and experimental means indicated by yellow pins. The Høvsøre mast is encircled by a red ellipse. The white solid boxes indicate the boundaries of the finest WRF grid projected onto the test site ($\Delta x = \Delta y = 1$ km).

tions have been used in horizontal and vertical space, respectively, to obtain values from the nearest grid points.

A four-domain nested mesoscale simulation set-up, shown in Figure 8.33, was used (details are provided in Table 8.5). An online mesoscale-microscale coupling approach with four one-way nested domains provided by the WRF model was employed. Physical parameterizations include the Kain-Fritsch scheme for cumulus [153], the Thompson scheme for microphysics [339], the Noah land surface model [47] and the Rapid Radiative Transfer Model for General Circulation Models (RRTMG) [137]. Revised MM5 surface layer scheme was used on all domains [145] for the S-H PBL model, whereas other PBL schemes were used with their own surface layer schemes. The model top was placed at 100 hPa (about 20 km in altitude) for the GFS reanalysis data and 20 hPa (about 33 km in altitude) for the ERA5 reanalysis data. For the upper 5 km of the domain, a Rayleigh damping layer was used to dampen the spurious waves that could be reflected from the model top. All domains were spun up for 12 hours in order to achieve steady-state flow conditions and well-developed turbulent wind flow on all domains.

Due to the fact that the WRF PBL results are instantaneous values recorded every 10-min and experimental data consists of 10-min averages, no statistical metrics of the WRF PBL sensitivity analysis with respect to the experimental data were calculated. Instead, 30-hour time series of values of U, β, and T from the finest domain of the WRF model exported

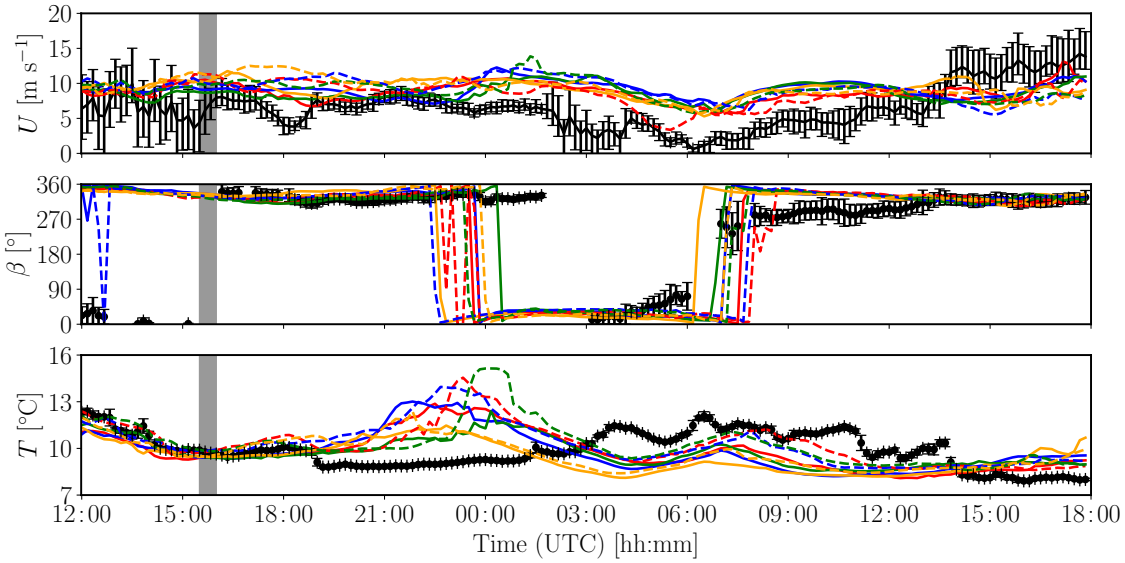

Figure 8.35: Time series of wind speed, U (first row), wind direction, β (second row), and temperature, T (third row), at 80 m from numerical results corresponding to WRF domain d04 exported every 10 s, and 10-min average experimental data from the Høvsøre mast. t (UTC) stands for Coordinated Universal Time in hours and minutes. (——) with vertical bars correspond to experimental data with minimum and maximum values. (——), (——), (——), and (——) denote the predictions by the MYJ, MYNN, S-H, and QNSE models using GFS reanalysis data, respectively, whereas (- - -), (- - -), (- - -), and (- - -) denote the predictions by the same models using ERA5 reanalysis data. Gray shaded region depicts the period of interest in the WLGL simulations described in the following section.

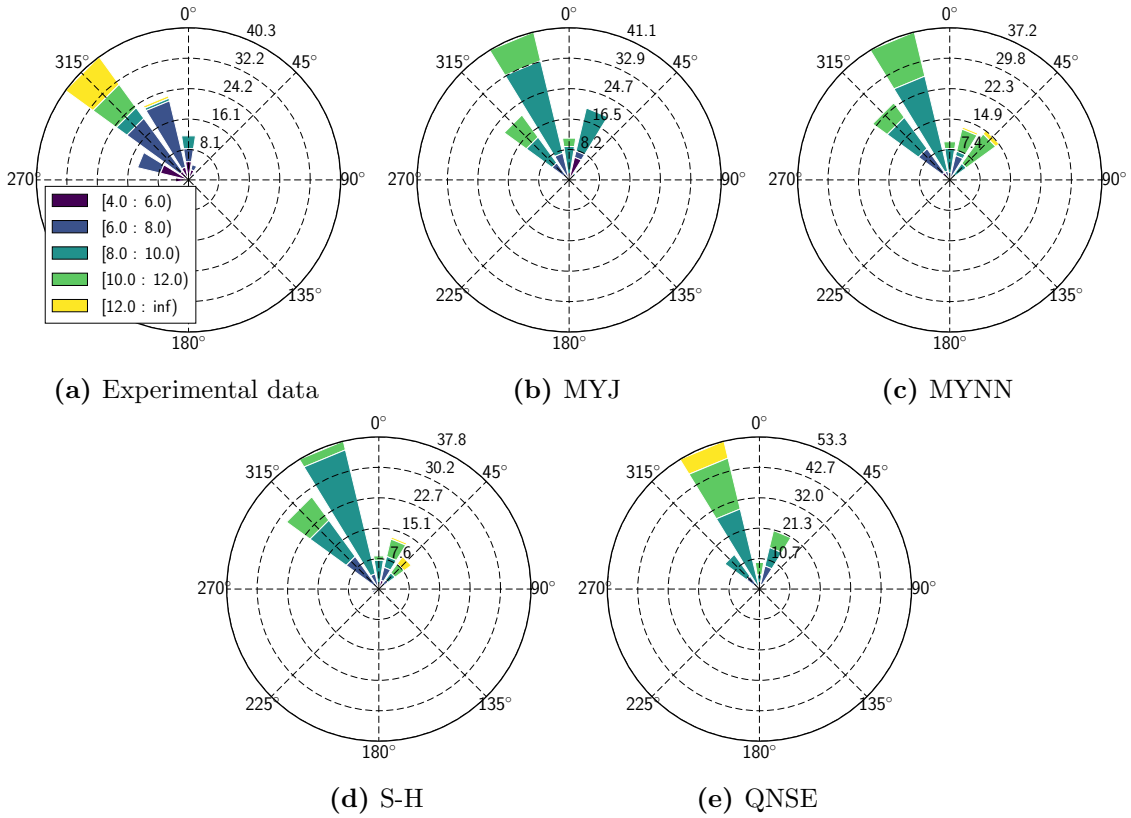

(a) Experimental data **(b)** MYJ **(c)** MYNN

(d) S-H **(e)** QNSE

Figure 8.36: Wind rose of 10-min average wind speeds observed at the meteorological mast at 80 m for the periods between 30/05/2006 12:00 (UTC) and 31/05/2006 18:00 (UTC) (a) and wind roses of simulated 10-min instantaneous winds at 80 m at the same location and for the same time frame, using ERA5 reanalysis dataset, from the MYJ (b), MYNN (c), S-H (d), and QNSE (e) WRF PBL models. 0° and 270° denote the north and west directions, respectively. Increasing numbers in the radial direction represent the probability of the event (in percent) occurring during the period of interest, with a total of 180 10-min periods.

every 10 s and 10-min averages from the experimental data, given in Figure 8.35, were compared qualitatively. The PBL model estimations of U, using ERA5 and GFS reanalysis, replicate a similar trend observed during measurements, with slight overestimation in the first 24 hours. As of 31/05/2006 at 14:00 (UTC), all PBL schemes underestimate the horizontal wind speed of about $\sim$4 m s^{-1}. For wind direction, all models forced with GFS and ERA5 reanalysis datasets agree reasonably well with the experimental data during the period of interest, with an overestimation of about $\sim 90°$ between 07:00 (UTC) and 14:00 (UTC) on 31/05/2006. This phenomenon could be attributed to the night/morning transition during which the characteristics and state of the PBL undergo intense evolution, possibly resulting in changes in wind direction and wind speed. For temperature, all PBL schemes provide accurate enough estimates within the first six hours of simulation on 30/05/2006; however, large deviations were observed as of 18:00 (UTC) on the same day, yielding an average standard deviation of about $\sim$4°C between 19:00 (UTC) on 30/05/2006 and 03:00 (UTC) on 31/05/2006. After, all models show a similar trend, underestimating the experimental data by $\sim$3°C on average.

As stated by Peña et al. [261], according to a wind climate analysis conducted for the period between 2005 and 2013 at Høvsøre, northwest winds prevail in the Høvsøre site, so the North Sea affects most of the winds. North winds are rare; therefore, wakes from turbines at the Høvsøre mast location are seldom observed. Besides, the authors have revealed that unstable ABL conditions were mostly observed around midday, while stable ABL conditions dominate the nighttime, as anticipated.

Figure 8.36 illustrates the wind roses of 10-min average wind speeds observed at the meteorological mast at 80 m over a period of thirty hours and WRF PBL model estimates of 10-min instantaneous wind speed at the same location and for the same time frame, using GFS reanalysis dataset. As illustrated in Figure 8.36a, $\sim$40% of the prevailing winds at 80 m blew from the northwest (i.e., 315°) during this particular sampling period, justifying the previous wind climate observations reported in Peña et al. [261]. The winds blew from the north $\sim$8% of the time. Among all PBL model results shown in (Figures 8.36b to 8.36e), the S-H PBL model gave the best estimations of the prevailing wind direction and wind speed results, with least errors, compared to the experimental data and other PBL schemes, either using GFS or ERA5 reanalysis dataset. Therefore, a combination of the S-H PBL scheme and the ERA5 reanalysis dataset, along with suitable atmospheric physics parameterizations, has been employed in subsequent multi-scale simulations, leveraging the ERA5 dataset's higher spatio-temporal resolution.

Mesoscale-microscale coupling using the WRF-LES model

The turbulent wind flow field required for the aerodynamic and aeroacoustic analysis of the SWT-2.3-93 WT was provided by mesoscale-microscale coupled wind turbine simulations of Høvsøre Wind Turbine Test Center for a pre-selected measurement period took place in May 30$^{\text{th}}$, 2006, between 15:34 and 16:00 (UTC). As previously discussed, the WRF model's inlet and lateral boundary conditions were established using ERA5 reanalysis data. However, a prior sensitivity analysis indicated that the combination of the GFS reanalysis dataset with the S-H PBL scheme yielded slightly improved results, particularly for hub height wind speeds, during the relevant time stamp.

In mesoscale ABL simulations (WRF) or mesoscale-microscale coupled ABL simulations (WRF-LES), the atmosphere is dynamically downscaled to the field of interest by forcing all necessary turbulent information from very large spatial scales to smaller scales where microscale effects become dominant. The number of domains used in the WRF-LES nested domain set-up mainly depends on the spatial resolution and nesting ratio. For instance, simulating a region with a horizontal resolution of several hundred meters requires at least four nested domains, starting with mesoscale domains with a spatial resolution of a few kilometers coupled with microscale domains.

As described in Section 8.1.3, a similar five-domain nested multi-scale simulation set-up for the WLGL model shown in Figure 8.3 was utilized (details are provided in Table 8.6). An online mesoscale-microscale coupling approach with five one-way nested domains, provided

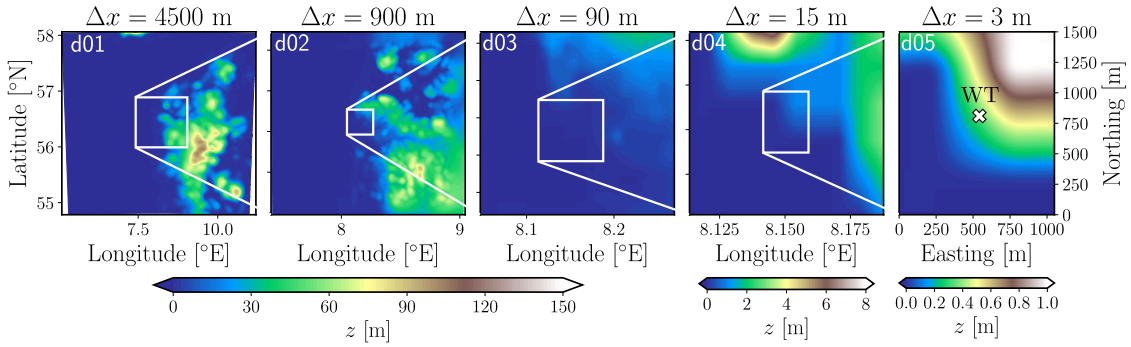

Figure 8.37: Nested domain configuration from the multi-scale WRF-LES simulation. All nested domains centered on the Høvsøre test site are colored by terrain height where $z = 0$ m corresponds to sea level. The five domains have resolutions of 4500 m, 900 m, 90 m, 15 m, and 3 m. Domain dimensions and other model configuration parameters are given in Table 8.6.

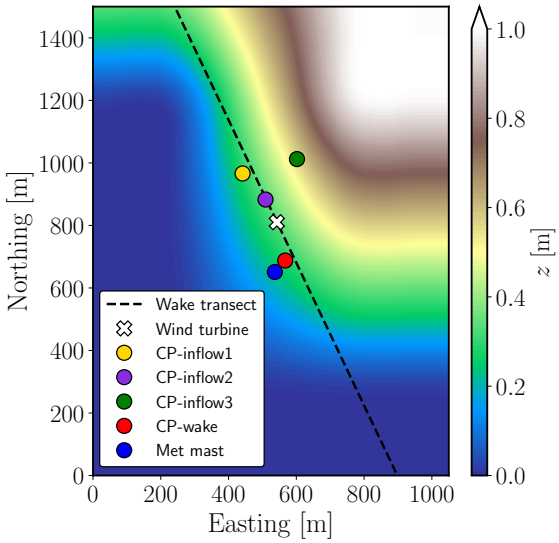

Figure 8.38: Illustration of the finest-resolution WRF-LES domain (WRF-LES-d05) colored by terrain height. (**- - -**) line denotes the wake transect, whereas the solid white cross depicts the location of the SWT-2.3-93 WT. The filled circles show the locations of the control points and the Høvsøre mast. CP stands for the control point.

by the WRF model, was utilized.

Mesoscale simulations were performed with two nested domains, with horizontal resolutions of $\Delta x = 4500$ m and 900 m, using the S-H PBL scheme. Three microscale domains, with horizontal resolutions of $\Delta x = 90$ m, 15 m, and 3 m, respectively, were run in LES mode using a 1.5-order TKE SFS turbulence scheme [71]. Vertical grid nesting was applied to all domains to allow for vertical grid refinement over nested domains, by reducing the overall time required to run the model. The nested domain configuration is shown in Figure 8.37.

With regard to temporal discretization and physical parameterizations, a set-up similar to that previously described in Section 8.1.3 was employed. The model top was placed

at 175 hPa (about 12.6 km in altitude) and no shading effects on the surface heat flux were enabled. The CPM was applied to trigger the generation of realistic atmospheric turbulence on the LES domains. The default USGS land use types and terrain data were used to obtain surface roughness lengths and resolve flow features at the test site. The same procedure as described in Section 8.1.3 was employed in order to generate well-developed fine-scale turbulent wind flow on all domains.

Validation of the ABL flow in the Høvsøre test site

The WRF-LES results were compared with the experimental data collected during the measurement campaign at Høvsøre in order to assess the accuracy of the WRF-LES model prior to analyzing the ABL flow-wind turbine interaction and aeroacoustic performance of the wind turbine. Since the available experimental data comprises 10-min averages, the time series of observed weather data are given with minimum and maximum values denoted by vertical error bars in Figure 8.39. The WRF-LES outputs are recorded every time step during the 30-min simulation period, corresponding to a sampling frequency of 200 Hz.

Long-term observations and wind climate simulations using WRF have shown that prevailing winds, in almost all cases, come from the northwest due to the North Sea and are very unlikely to blow from the north [261]. Nevertheless, the 10-min averages of wind direction from the Høvsøre mast at 80 m, illustrated in Figure 8.39, have shown that, during the period of interest, northerly winds were dominant, possibly causing weather measurements taken at the mast position to be affected by wakes from wind turbines. This is also visible in WRF-LES results of wind speed and wind direction at 80 m, recorded at a control point in the wake of the wind turbine, close to the Høvsøre mast (see Figure 8.38). WRF-LES estimates of wind speed and wind direction at 80 m in the wake of the wind turbine match fairly well with the experimental data. The WRF-LES results, determined at various locations upstream of the wind turbine, do not show large deviations from the mean values, as observed in the experimental data, supporting the possibility that wind turbine wakes may have an effect on the measured weather data. Since the WRF-LES underestimated the wind direction at 80 m, at the mast location, by about 10°, which means that the model predicted that winds were generally blowing from the northwest,

Table 8.6: Domain dimensions and model configuration parameters for the analysis of the ABL flow at Høvsøre.

Domain	$N_x \times N_y \times N_z$	Δx [m]	Δz [m]	Δt [s]	Turb. model	CPM	Spin-up [min]
d01	$81 \times 81 \times 51$	4500	$\sim$75	24	S-H	No	600
d02	$111 \times 111 \times 71$	900	$\sim$60	4.8	S-H	No	600
d03	$151 \times 151 \times 111$	90	$\sim$30	0.4	1.5-order TKE	Yes	210
d04	$301 \times 301 \times 141$	15	$\sim$10	0.05	1.5-order TKE	Yes	30
d05	$351 \times 501 \times 221$	3	$\sim$3	0.005	1.5-order TKE	Yes	10

Note. N_x, N_y, and N_z stand for the number of grid points whereas $\Delta x, \Delta y$, and Δz represent the spatial grid resolutions in the x, y, and z directions, respectively. Note that $\Delta x = \Delta y$ and Δz is set close to the values given in the table, because of WRF's terrain-following eta coordinate system in the vertical direction. Δt is the computational time-step size. CPM denotes the Cell Perturbation Method [234].

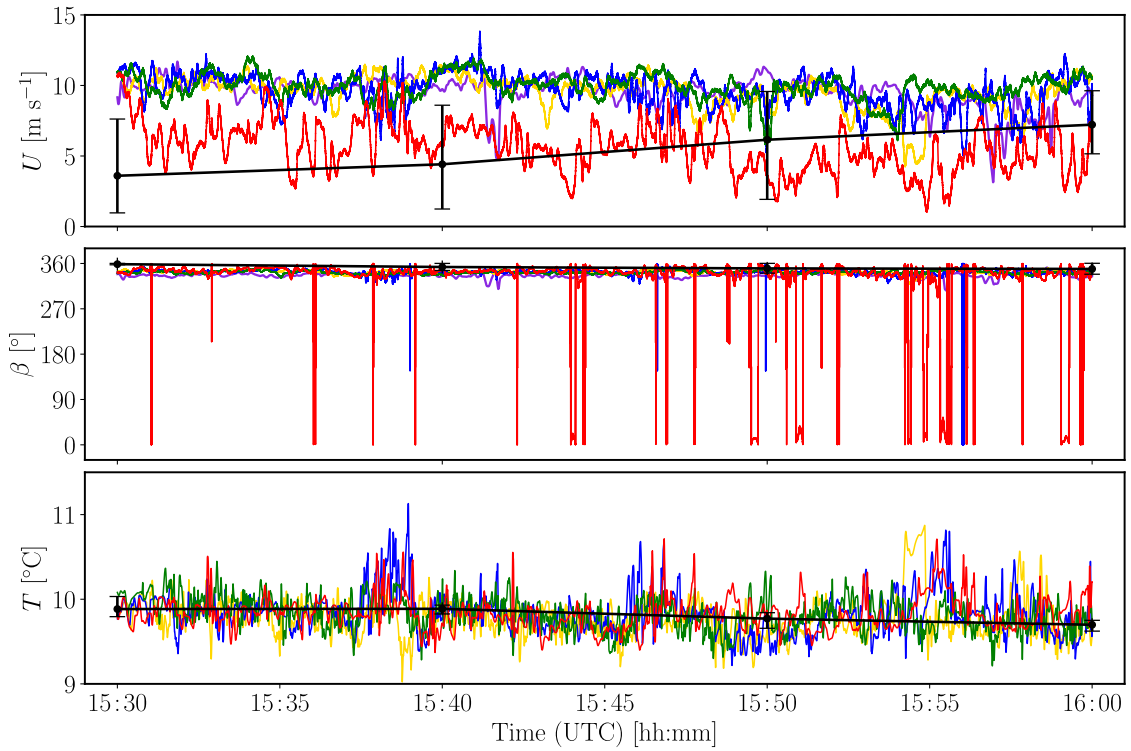

Figure 8.39: Time series of wind speed, U (first row), wind direction, β (second row), and temperature, T (third row), at 80 m from numerical results corresponding to WRF-LES-d05, and 10-min average experimental data from the Høvsøre mast. t (UTC) stands for Coordinated Universal Time in hours and minutes. (|) with horizontal bars correspond to experimental data with minimum and maximum values. (—) denotes the WRF-LES results at the met mast location, (—) denotes the results at a control point upstream of the wind turbine in the northwest direction (CP-inflow1), (—) stands for the results at a point one rotor diameter upstream of the wind turbine (CP-inflow2), (—) denotes the results at a control point upstream of the wind turbine in the northeast direction (CP-inflow3), and (—) denotes the model predictions at a control point in the wake of the wind turbine close to the met mast (CP-wake). The reader is referred to Figure 8.38 for the layout of the WRF-LES control points.

the simulated wind turbine wake did not affect the wind speed at 80 m at the actual met mast location. Time series of modeled and observed temperature agree quite well, despite small deviations of about 1°C.

Figure 8.40 shows vertical profiles of time-averaged wind speed, $\overline{U}$, wind direction, $\overline{\beta}$, and temperature, $\overline{T}$, as well as turbulence intensity, $\overline{TI}$, from numerical results corresponding to WRF-LES-d05, and experimental data from the Høvsøre mast. WRF-LES results were obtained from time series, sampled at 200 Hz, whereas experimental data were obtained by averaging the 10-min averages over the period of interest. The undisturbed wind speed profiles overestimate the measured data; however, the wind speed profile obtained in the wake of the wind turbine matches the mean values of the experimental data above 60 m. This result evidences the influence of the wake on the wind speed measurements at the met mast location. In addition, the backward S-shaped profile in the measured wind speed indicates a deceleration of the wind speed along the wind turbine rotor during the